

# Robust Frequency-Calibrated Virtual EEG Channel Generation from Four Frontal Electrodes for Wearable EEG Augmentation

---

Minghao Xiao<sup>1,2</sup>

1 School of Biomedical Science and Engineering, South China University of Technology, Guangzhou 511442, China

2 School of Automation Science and Engineering, South China University of Technology, Guangzhou 510640, China

E-mail: 3098975303@qq.com

## Abstract

Low-channel wearable electroencephalography (EEG) is attractive for long-term monitoring, but four frontal electrodes provide only a sparse and spatially biased view of distributed scalp activity. We present FAVC-Net, a compact frequency-calibrated virtual-channel network that generates 13 unmeasured EEG channels from Fp1, Fp2, F7, and F8. The model combines shared multi-scale source encoding, source-state embeddings, target-conditioned signed source-block mixing, GATv2-based attention refinement, attention-consistent skip fusion, and weak Welch power spectral density calibration. Rather than treating sparse-to-dense EEG generation as a purely waveform-matching task, the framework jointly emphasizes amplitude fidelity, spectral allocation, channel-frequency texture, and robustness to corrupted wearable inputs. On the PRED+CT dataset, FAVC-Net achieved the best joint waveform-spectral operating point among neural and interpolation baselines. Its time-domain gains were modest, whereas log-spectral distance and PSD KL divergence were reduced by 30.09% and 37.98% relative to the strongest non-FAVC comparator. Under wearable-like source perturbations, the model preserved spectral fidelity and resisted spectral collapse. These results support virtual EEG channel generation as a dual-domain augmentation problem, while emphasizing that generated posterior and parietal channels should be interpreted as frequency-calibrated representations derived from sparse frontal measurements rather than as independent physical recordings.

## Keywords

Electroencephalography; Virtual channels; Wearable EEG; Sparse-to-dense reconstruction; Robustness

## 1. Introduction

Electroencephalography (EEG) provides millisecond-scale access to neural dynamics and remains important in neuroengineering, affective computing, brain-computer interfaces, and quantitative neurophysiology [6, 24]. Dense or clinical-grade montages provide broad scalp coverage, but their setup time, electrode maintenance, cost, and wearing burden limit ambulatory and long-term wearable use. Four-frontal systems are therefore attractive for practical monitoring, yet they observe only a partial view of the scalp field. This limitation matters because many task- and state-related EEG signatures are distributed across frontal, temporal, central, and parietal regions rather than being fully represented by isolated frontal amplitudes [1, 3, 11, 21].

Virtual EEG channel generation addresses this sparse-sensing problem by estimating unmeasured channels from measured channels. Classical interpolation methods such as nearest-neighbor interpolation, inverse-distance weighting, and spherical splines are transparent and useful when a dense montage contains only a small number of defective electrodes [8, 9, 12, 13, 22]. Four frontal electrodes, however, do not define a conventional bad-channel interpolation setting. They define an

underdetermined conditional reconstruction problem in which 13 target channels must be inferred from a spatially clustered sparse montage. In this regime, the mapping depends on source state, reference effects, oscillatory regime, subject variability, and nonstationary source-target coupling, not only on geometric distance.

Recent learned approaches have explored EEG spatial super-resolution, channel restoration, attention-based interpolation, state-space models, Transformer architectures, diffusion models, and attention U-Nets [5, 7, 16-19, 26, 27, 30-33]. These studies establish the feasibility of learned dense-channel generation, but they also reveal an evaluation gap. Many comparisons emphasize waveform reconstruction scores, whereas wearable EEG analysis often relies on PSD shape, band powers, spectral slope, regional energy gradients, and channel-frequency texture [10, 15, 23, 29]. A generated channel can achieve acceptable amplitude error or Pearson correlation while misallocating spectral energy or producing overly homogeneous virtual channels. Sparse-to-dense EEG generation should therefore be treated as a dual-domain reconstruction task.

We propose FAVC-Net, a frequency-calibrated virtual-channel network that generates 13 virtual EEG channels from Fp1, Fp2, F7, and F8. The design follows three principles. First, source-to-target mapping should be state-dependent because the same frontal electrodes can reflect different oscillatory regimes across windows. Second, generation should be target-specific because frontal, central, temporal, and posterior targets require different source-response rules. Third, source mixing should allow signed contributions because EEG referencing and phase relationships can induce negative dependencies that are suppressed by positive-simplex attention.

The contributions are threefold: (i) a compact target-conditioned architecture for four-frontal-to-multichannel EEG augmentation; (ii) a dual-domain training and evaluation strategy that treats waveform fidelity and spectral-topographic fidelity as joint criteria; and (iii) a corrupted-source robustness analysis showing that the model preserves absolute spectral fidelity and resists spectral collapse under wearable-relevant perturbations. The claim is intentionally bounded: generated channels are deterministic, frequency-calibrated virtual representations of sparse frontal measurements, not independent substitutes for physically recorded posterior electrodes.

## 2. Methods

### 2.1 Data, channel selection, and preprocessing

The primary reconstruction experiment used the PRED+CT EEG database released by Cavanagh et al. [4]. The database contains recordings from 119 subjects performing a probabilistic learning task. According to the dataset description used in this analysis, participants comprised 74 male and 45 female subjects aged 18-24 years; EEG was recorded at 500 Hz from 66 electrodes arranged according to the international 10-20 system [13]. Trait-anxiety categories based on the Spielberger Trait Anxiety Inventory were recorded in the database [25], but these labels were not used for reconstruction training, validation, testing, model selection, robustness analysis, or virtual-channel generation.

Seventeen channels were selected to cover frontal, temporal, central, and parietal regions: Fp1, Fp2, F7, F3, Fz, F4, F8, T3, C3, Cz, C4, T4, T5, P3, Pz, P4, and T6. The measured source set was Fp1, Fp2, F7, and F8, representing a practical four-frontal wearable layout. The target set contained the remaining 13 channels. Signals were band-pass filtered from 0.5 to 45 Hz and segmented into 3000-sample windows, corresponding to 6 s at 500 Hz. The reconstruction split was strictly subject-independent: 95 subjects and 950 segments were used for training, 11 subjects and 110 segments for validation, and 13 subjects and 130 segments for testing. Channel-wise standard deviations were computed from the training subjects only and were used for normalization and normalized MAE reporting. Acquisition, montage, filtering, segmentation, and split information are reported in line with general EEG/MEG publication recommendations [14].

## 2.2 Problem formulation

Let  $x_i \in \mathbb{R}^T$  denote the  $i$ th measured source channel, ordered as Fp1, Fp2, F7, and F8. The sparse source segment and target montage are

$$X = [x_1, x_2, x_3, x_4]^T \in \mathbb{R}^{4 \times T}, \quad Y = [y_1, \dots, y_{13}]^T \in \mathbb{R}^{13 \times T}.$$

The generator  $G_\theta$  estimates the unmeasured targets from the measured sources and target identity:

$$\hat{Y} = G_\theta(X, q) = [\hat{y}_1, \dots, \hat{y}_{13}]^T \in \mathbb{R}^{13 \times T},$$

where  $q$  denotes the target identity or the target-conditioned parameters used by the generator. At inference, target-channel waveforms are unavailable. The model must therefore infer target-specific source mixtures from measured sources and electrode identity alone, making the task a conditional sparse-to-dense mapping rather than supervised denoising with target-channel input.

## 2.3 FAVC-Net architecture

FAVC-Net is shown in Fig. 1. Each source channel is passed through the same one-dimensional multi-scale encoder. The encoder has four stride-2 stages and parallel temporal kernels of length 3, 5, and 9, with output widths 32, 64, 128, and 256. Weight sharing keeps the model compact and prevents the four measured sources from being represented by unrelated feature extractors, while the multi-scale kernels expose local transients, rhythmic envelopes, alpha/beta oscillations, and nonstationary artifacts at different receptive-field widths.

For source  $i$ , the shared encoder produces

$$h_i = E_\phi(x_i) \in \mathbb{R}^{C \times L}, \quad i = 1, \dots, 4.$$

The final  $C = 256$  channels are divided into  $B = 32$  latent blocks. This block partition lets a virtual target select source contributions at a frequency- and morphology-sensitive latent-block level instead of relying on a single scalar source weight.

The current source state is summarized by temporal moments and extrema of the encoded feature map:

$$s_i = \left[ \mu_\tau(h_i), \sigma_\tau(h_i), \max_\tau h_i, \min_\tau h_i \right].$$

A compact identity network maps this descriptor to a 32-dimensional source-state embedding:

$$e_i = \text{LN}(W_2 \delta(\text{BN}(W_1 s_i + b_1)) + b_2) \in \mathbb{R}^{32}, \quad E_s = [e_1; e_2; e_3; e_4].$$

Here  $\delta(\cdot)$  is a pointwise nonlinearity, BN denotes batch normalization, and LN denotes layer normalization. The embeddings summarize the state of the measured sparse montage and drive attention generation rather than using target waveforms, which are unavailable at inference.

For virtual target  $t$ , a target-private first layer followed by a shared second layer produces source-by-block attention scores:

$$A_t = \text{reshape}_{4 \times B} \left( W_a^{(2)} \delta \left( W_{a,t}^{(1)} E_s + b_{a,t}^{(1)} \right) + b_a^{(2)} \right), \quad A_t \in \mathbb{R}^{4 \times B}.$$

The private first layer gives each virtual electrode a distinct source-response rule, while the shared second layer encourages the latent blocks to retain comparable meaning across targets. This balances specialization and statistical efficiency: Fz, T3, Cz, Pz, and T6 should not share one global source mixture, but all targets are still inferred from the same four measured sources.

The 13 virtual targets are then treated as graph nodes. For GATv2 refinement, each source-by-block attention tensor is flattened into a node feature. This refinement follows graph-attention principles [28] and uses the more expressive GATv2 formulation [2]:

$$z_t = \text{flatten}(A_t) \in \mathbb{R}^{4B}.$$

Approximate 10-20 coordinates define a weak spatial prior over virtual targets:

$$P_{tu} = \exp\left(-\frac{\|p_t - p_u\|_2^2}{\tau_p}\right),$$

where  $p_t$  and  $p_u$  are two-dimensional electrode coordinates and  $\tau_p$  controls the spatial scale. The prior is used only as a neighborhood mask and a small logit bias; it is not an output-voltage smoothing constraint. For connected nodes  $u \in \mathcal{N}(t)$ , the GATv2 refinement logit is

$$r_{tu} = a_g^\top \text{LeakyReLU}(W_s z_t + W_u z_u + b_g) + \lambda_g \log(P_{tu} + \epsilon),$$

and the attention coefficient is

$$\alpha_{tu} = \frac{\exp(r_{tu})}{\sum_{v \in \mathcal{N}(t)} \exp(r_{tv})}.$$

The graph message and gated residual update are

$$m_t = \sum_{u \in \mathcal{N}(t)} \alpha_{tu} W_m z_u, \quad \gamma_t = \sigma(W_\gamma [z_t \parallel m_t] + b_\gamma), \quad z_t^{\text{ref}} = z_t + \gamma_t \odot m_t.$$

The refined vector is reshaped back to a source-by-block tensor before source aggregation. Thus, GATv2 exchanges information about plausible source-block patterns among virtual targets, but it does not average reconstructed voltages across neighboring electrodes. This distinction is important because direct smoothing may improve visually pleasing topographies while degrading channel-specific spectral texture.

After graph refinement, scores are normalized over the four source channels by signed  $L_1$  normalization rather than softmax:

$$\tilde{a}_{tib} = \frac{a_{tib}^{\text{ref}}}{\sum_{j=1}^4 |a_{tjb}^{\text{ref}}| + \epsilon}, \quad i = 1, \dots, 4, \quad b = 1, \dots, B.$$

Let  $b(k)$  map encoder channel  $k$  to its latent block. The target-specific latent state is

$$\tilde{h}_{t,k,:} = \sum_{i=1}^4 \tilde{a}_{ti,b(k)} h_{i,k,:}.$$

Signed normalization allows negative or phase-inverted source-target relationships under a fixed EEG reference, which would be suppressed by positive-simplex softmax attention. A shared  $1 \times 1$  convolutional adapter and shared transposed-convolution decoder reconstruct the 13 virtual waveforms. Shallow encoder features are compressed according to learned attention magnitude and fused into decoder stages as attention-consistent skip connections. The final implementation contains 912,770 trainable parameters.

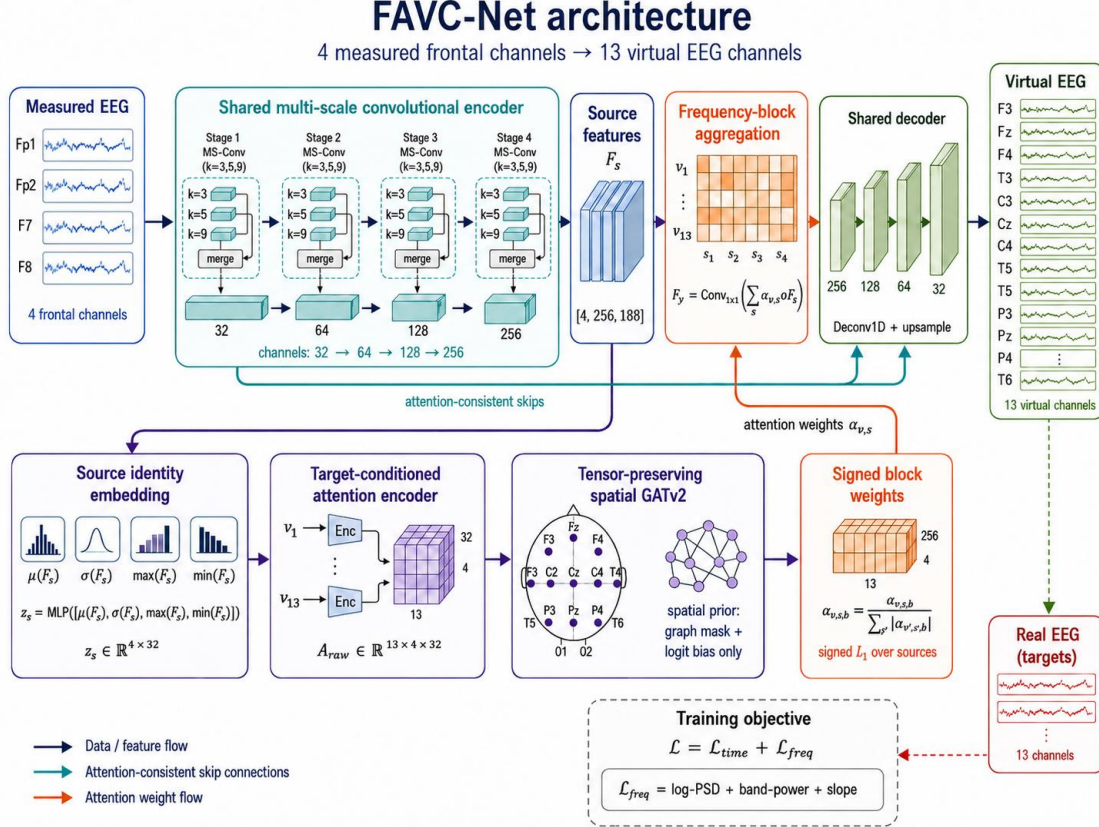


**Fig. 1 FAVC-Net architecture.** Four frontal source channels are encoded by a shared multi-scale encoder. Source-state embeddings drive target-conditioned signed attention. The source-by-block attention tensor is refined over virtual targets by GATv2 and then used for signed aggregation, attention-consistent skip fusion, and shared decoding into 13 virtual EEG channels.

## 2.4 Training objective and reconstruction metrics

The training objective combines a dominant normalized waveform term with weak frequency-domain calibration:

$$\mathcal{L} = 0.90 \mathcal{L}_{\text{wave}} + 0.10 \mathcal{L}_{\text{PSD}}.$$

The waveform term is a normalized absolute reconstruction loss:

$$\mathcal{L}_{\text{wave}} = \frac{1}{13T} \sum_{c=1}^{13} \sum_{t=1}^T \frac{|\hat{y}_{c,t} - y_{c,t}|}{\sigma_c + \epsilon},$$

where  $\sigma_c$  is the training-set standard deviation of target channel  $c$ . The PSD term is computed from differentiable Welch estimates over 0.5-45 Hz. For a Hann window  $w$ , sampling frequency  $f_s$ , and windowed frame  $x_{c,n}$ , the PSD estimate is

$$S_c(f) = \frac{1}{N} \sum_{n=1}^N \frac{|\mathcal{F}\{w \odot x_{c,n}\}(f)|^2}{f_s \sum_{\ell} w_{\ell}^2}.$$

The implemented PSD calibration combines log-PSD shape, relative physiological band allocation, and spectral-slope consistency:

$$\mathcal{L}_{\text{PSD}} = \lambda_{\log} \|\log(\hat{S} + \epsilon) - \log(S + \epsilon)\|_1 + \lambda_{\text{band}} \|\hat{\rho} - \rho\|_1 + \lambda_{\text{slope}} \|\hat{\beta} - \beta\|_1.$$

The calibration term is intentionally weak: it is designed to correct spectral allocation without allowing PSD matching to dominate sample-wise waveform reconstruction. A validation sweep showed a smooth trade-off in which increasing the PSD weight gradually improved spectral metrics while slightly reducing waveform fidelity. The 0.90/0.10 setting was selected as a balanced operating point rather than as a narrowly tuned optimum.

Four reconstruction metrics were used. Normalized MAE measures amplitude error relative to training-set channel standard deviation:

$$\text{nMAE} = \frac{1}{13T} \sum_{c=1}^{13} \sum_{t=1}^T \frac{|\hat{y}_{c,t} - y_{c,t}|}{\sigma_c + \epsilon}.$$

Pearson correlation measures phase-sensitive waveform agreement:

$$r = \frac{1}{13} \sum_{c=1}^{13} \frac{\sum_t (\hat{y}_{c,t} - \bar{\hat{y}}_c) (y_{c,t} - \bar{y}_c)}{\sqrt{\sum_t (\hat{y}_{c,t} - \bar{\hat{y}}_c)^2 \sum_t (y_{c,t} - \bar{y}_c)^2 + \epsilon}}.$$

Log-spectral distance compares the absolute log-power envelope:

$$\text{LSD} = \sqrt{\frac{1}{13|\mathcal{F}|} \sum_{c=1}^{13} \sum_{f \in \mathcal{F}} [\log(\hat{S}_c(f) + \epsilon) - \log(S_c(f) + \epsilon)]^2}.$$

PSD-normalized KL divergence compares within-channel frequency allocation:

$$p_c(f) = \frac{S_c(f)}{\sum_{f' \in \mathcal{F}} S_c(f') + \epsilon}, \quad \hat{p}_c(f) = \frac{\hat{S}_c(f)}{\sum_{f' \in \mathcal{F}} \hat{S}_c(f') + \epsilon},$$

$$\text{KL} = \frac{1}{13} \sum_{c=1}^{13} \sum_{f \in \mathcal{F}} p_c(f) \log \frac{p_c(f) + \epsilon}{\hat{p}_c(f) + \epsilon}.$$

Together, these metrics separate amplitude fidelity, phase-sensitive waveform agreement, absolute log-power structure, and normalized spectral-shape similarity. Raw-scale MAE was derived from the same training-set channel standard deviations for all methods, so differences in raw MAE are not caused by method-specific rescaling.

## 2.5 Baselines and implementation protocol

FAVC-Net was compared with neural and interpolation baselines: Deep-CNN, GN, EC-Informer, VEEG-A-U-Net, ESTformer, inverse-distance weighting, spherical-spline interpolation, and nearest-neighbor interpolation. All methods used the same source channels, target channels, subject-level split, and evaluation metrics. Neural methods were summarized as mean  $\pm$  standard deviation across repeated runs. FAVC-Net was optimized with AdamW [20], learning rate  $1.0 \times 10^{-4}$ , weight decay  $1.0 \times 10^{-5}$ , batch size 16, gradient clipping at 1.0, ReduceLROnPlateau scheduling, and early stopping.

## 2.6 Checkpoint-only robustness to wearable-like source-channel perturbations

To test whether virtual-channel generation remains useful when measured frontal inputs are corrupted, robustness analysis was performed in a checkpoint-only manner. Saved checkpoints were evaluated without retraining, fine-tuning, noise-specific calibration, or post hoc checkpoint selection. Perturbations were applied only to the four measured source channels, whereas the 13 target channels remained clean. The experiment therefore measured the ability to reconstruct the clean target montage from imperfect wearable inputs, not the ability to copy noise into the targets.

The main text focuses on four perturbations that are practically relevant after routine preprocessing: moderate EMG-like high-frequency bursts, 0.5-s source-channel dropout,  $\pm 20\%$  channel-wise gain mismatch, and moderate mixed wearable stress. The moderate mixed condition applied AWGN at 10 dB, EMG bursts at 10 dB with two bursts of 0.30-0.80 s and channel probability 0.50, one 0.50-s source-channel dropout, and  $\pm 20\%$  gain mismatch. Absolute noisy-condition performance was used as the primary robustness endpoint because percentage degradation can over-penalize a model that starts from a substantially lower clean spectral error.

The perturbations were generated reproducibly from the split seed, condition name, and repeat index. AWGN was scaled per sample and source channel according to source RMS and the specified SNR:

$$\sigma_{b,c} = \frac{\text{RMS}(x_{b,c,:})}{\sqrt{10^{\text{SNR}_{\text{dB}}/10}}}, \quad x'_{b,c,t} = x_{b,c,t} + \varepsilon_{b,c,t}, \quad \varepsilon_{b,c,t} \sim \mathcal{N}(0, \sigma_{b,c}^2).$$

EMG-like bursts were generated as 20-45 Hz band-limited noise multiplied by a Hann temporal envelope and RMS-calibrated to the target SNR. Dropout selected one source channel and set a contiguous temporal window to zero,

$$x'_{b,c,t} = m_{b,c,t} x_{b,c,t}, \quad m_{b,c,t} \in \{0,1\},$$

and gain mismatch multiplied each source by a random channel-wise factor:

$$g_{b,c} \sim \text{Uniform}(1 - \rho, 1 + \rho), \quad x'_{b,c,t} = g_{b,c} x_{b,c,t}.$$

Robustness was quantified by LSD, PSD KL divergence, spectral-collapse index (SCI), and channel-frequency texture correlation (CFTC). CFTC is the Pearson correlation between vectorized log-PSD tensors of predicted and true target channels:

$$\text{CFTC}_b = \text{corr}(\text{flatten}\{\log(\hat{S}_b + \epsilon)\}, \text{flatten}\{\log(S_b + \epsilon)\}).$$

SCI measures whether predicted channels become spectrally over-homogeneous. For each subject-window  $b$  and all target-channel pairs  $i < j$ , the pairwise channel spectral distances are

$$D_b^{\text{pred}} = \frac{2}{C(C-1)} \sum_{i < j} \|\log(\hat{S}_{b,i} + \epsilon) - \log(\hat{S}_{b,j} + \epsilon)\|_2,$$

$$D_b^{\text{true}} = \frac{2}{C(C-1)} \sum_{i < j} \|\log(S_{b,i} + \epsilon) - \log(S_{b,j} + \epsilon)\|_2, \quad C = 13.$$

The pairwise collapse component penalizes loss of between-channel spectral diversity:

$$\text{SCI}_b^{\text{pair}} = \max\left(1 - \frac{D_b^{\text{pred}}}{D_b^{\text{true}} + \epsilon}, 0\right).$$

For band-topographic variance, let  $\mathcal{B}_k$  denote the delta, theta, alpha, beta, or low-gamma band. Band powers and variance ratios are

$$\text{BP}_{b,c,k}^{\text{pred}} = \log\left(\sum_{f \in \mathcal{B}_k} \hat{S}_{b,c}(f) + \epsilon\right), \quad \text{BP}_{b,c,k}^{\text{true}} = \log\left(\sum_{f \in \mathcal{B}_k} S_{b,c}(f) + \epsilon\right),$$

$$\text{BTVR}_{b,k} = \frac{\text{std}_c(\text{BP}_{b,c,k}^{\text{pred}})}{\text{std}_c(\text{BP}_{b,c,k}^{\text{true}} + \epsilon)}.$$

The topographic-collapse component and implemented SCI are

$$\text{SCI}_b^{\text{topo}} = \frac{1}{K} \sum_{k=1}^K \max(1 - \text{BTVR}_{b,k}, 0), \quad \text{SCI}_b = 0.5 \text{SCI}_b^{\text{pair}} + 0.5 \text{SCI}_b^{\text{topo}}.$$

Lower SCI indicates less spectral collapse. Subject-level summaries were obtained by first aggregating segments within each subject; the paired mixed-stress comparison used Wilcoxon signed-rank tests against the strongest non-FAVC comparator.

## 2.7 Exploratory external representation transfer check

An auxiliary downstream experiment examined whether generated channels carry useful representation value outside the reconstruction dataset. The external recordings came from the low-cost, wireless, four-channel EEG measurement system for virtual-reality environments described by Yu and Guo [34]. Thirty-four subjects were retained after exclusion, each contributing 30 six-second windows. The device recorded four frontal channels at 250 Hz; AF7 and AF8 were used as lateral-frontal proxies for F7 and F8. External signals were filtered using the same passband logic, resampled to the 500 Hz/3000-sample model input length, and normalized with the PRED+CT training-set channel statistics stored in the reconstruction checkpoint. The generator was used zero-shot and was never updated with external data.

The external dataset contained only the four measured frontal channels and therefore had no ground-truth recordings for the 13 target channels. Consequently, no external target-channel waveform, target-channel statistic, or target-derived preprocessing parameter was available to the generator or to the downstream pipeline. Five channel configurations were evaluated: D0, real four-channel features only; D1, real channels plus 13 FAVC-generated virtual-channel features; D2, generated virtual channels only; D3, real channels plus duplicated/proxy-expanded channels; and D4, real channels plus phase-random pseudo-channels. D3 and D4 served as negative controls for dimensionality expansion and arbitrary pseudo-channel spectra. This experiment is reported as exploratory representation-transfer evidence rather than clinical validation.

Feature extraction, feature screening, dimensionality reduction, and classifier training were performed strictly within each subject-held-out cross-validation fold. The held-out subject was excluded from ANOVA screening, PCA fitting, classifier training, and all model-selection operations in that fold. Labels were used only within the downstream training portion of each fold and were never used to train, tune, or select the virtual-channel generator. This design prevents target-channel leakage, subject leakage, and test-fold leakage while testing whether the generated montage can provide useful features beyond the measured frontal channels under device, montage, sampling-rate, and cohort mismatch.

## 3. Results

### 3.1 Overall dual-domain reconstruction performance

FAVC-Net achieved the best joint waveform-spectral operating point among the evaluated methods (Table 1). Relative to the strongest non-FAVC comparator for each metric, it reduced nMAE from 0.1497 to 0.1454, reduced raw MAE from 4.655  $\mu\text{V}$  to 4.518  $\mu\text{V}$ , and improved Pearson correlation from 0.6206 to 0.6258. These time-domain gains are deliberately interpreted as modest. The main advantage was spectral: LSD decreased from 0.9657 to 0.6751, and PSD KL divergence decreased from 0.1506 to 0.0934. Thus, the method’s contribution is not simply a lower pointwise error but a more faithful spectral-topographic representation under a comparable waveform-fidelity constraint.

The result is also parameter efficient. FAVC-Net used 0.913 million parameters, far fewer than GN, VEEG-A-U-Net, and Deep-CNN, while outperforming them in the combined metric set. The interpolation baselines remained useful references but were disadvantaged by the sparse and spatially clustered source montage. Their errors show that the task is not equivalent to replacing one missing electrode in a dense array; frontal-to-posterior inference requires learned conditional structure beyond smooth geometric interpolation.

**Table 1 Compact overall reconstruction performance on 13 virtual target channels. Values are mean  $\pm$  standard deviation; lower values are better except Pearson  $r$ .**

Method	Parameters	nMAE $\downarrow$	Raw MAE ( $\mu\text{V}$ ) $\downarrow$	Pearson $r$ $\uparrow$	LSD $\downarrow$	PSD KL $\downarrow$
FAVC-Net	912,770	0.1454 $\pm$ 0.0025	4.518 $\pm$ 0.079	0.6258 $\pm$ 0.0072	0.6751 $\pm$ 0.0023	0.0934 $\pm$ 0.0022
GN	4,913,473	0.1497 $\pm$ 0.0045	4.655 $\pm$ 0.138	0.6206 $\pm$ 0.0114	1.5574 $\pm$ 0.1146	0.1876 $\pm$ 0.0081
ESTformer	874,162	0.1536 $\pm$ 0.0032	4.777 $\pm$ 0.099	0.5804 $\pm$ 0.0119	1.7495 $\pm$ 0.0725	0.1883 $\pm$ 0.0025
VEEG-A-U-Net	5,940,161	0.1607 $\pm$ 0.0039	4.992 $\pm$ 0.122	0.5944 $\pm$ 0.0127	0.9657 $\pm$ 0.0468	0.1652 $\pm$ 0.0219
Deep-CNN	2,255,181	0.1620 $\pm$ 0.0059	5.038 $\pm$ 0.183	0.5924 $\pm$ 0.0096	1.2961 $\pm$ 0.1639	0.1506 $\pm$ 0.0120
EC-Informer	600,304	0.1651 $\pm$ 0.0062	5.141 $\pm$ 0.197	0.5321 $\pm$ 0.0340	2.1307 $\pm$ 0.1780	0.2846 $\pm$ 0.0351
IDW	0	0.3233 $\pm$ 0.0131	10.008 $\pm$ 0.411	0.3681 $\pm$ 0.0269	1.3078 $\pm$ 0.0691	0.2897 $\pm$ 0.0203
NNI	0	0.3341 $\pm$ 0.0143	10.350 $\pm$ 0.449	0.4126 $\pm$ 0.0194	1.4965 $\pm$ 0.0350	0.2462 $\pm$ 0.0231
SSI	0	0.5115 $\pm$ 0.0346	15.761 $\pm$ 1.068	0.4999 $\pm$ 0.0212	2.3992 $\pm$ 0.1318	0.2458 $\pm$ 0.0287

nMAE, normalized mean absolute error; MAE, mean absolute error; LSD, log-spectral distance; KL, PSD-distribution KL divergence.

### 3.2 Channel-wise observability and waveform visualization

Channel-wise results (Table 2) show a plausible observability gradient. Near-frontal targets F3, Fz, and F4 had the highest correlations because they are closest to the measured frontal sources and share frontal activity. Lateral temporal and central channels remained moderately recoverable. Posterior and parietal targets had lower phase-sensitive correlations, which is expected from four frontal sources. The representative overlay in Fig. 2 visually confirms that generated signals follow large-scale morphology and local waveform patterns in many channels, while posterior targets retain plausible but less phase-locked variability.

Raw MAE values varied across targets, reflecting both reconstruction difficulty and intrinsic channel amplitude scale. The high correlations for F3, Fz, and F4 should not be generalized to all targets, and the lower posterior correlations should not be interpreted as model collapse. They instead define the practical observability boundary of a four-frontal sensor layout. This boundary is useful for deployment because it indicates which virtual channels are most reliable for phase-sensitive analyses and which should be interpreted primarily as spectral-topographic representations.

**Table 2 Channel-wise FAVC-Net reconstruction results under the 0.90/0.10 objective.**

Channel	nMAE $\downarrow$	Raw MAE ( $\mu\text{V}$ )	Pearson $r$ $\uparrow$	Observability interpretation
F3	0.1298 $\pm$ 0.0028	4.170 $\pm$ 0.089	0.8820 $\pm$ 0.0037	Near-frontal; strong source observability
Fz	0.1205 $\pm$ 0.0015	3.870 $\pm$ 0.050	0.9025 $\pm$ 0.0018	Near-frontal; strong source observability
F4	0.1188 $\pm$ 0.0022	3.936 $\pm$ 0.073	0.9083 $\pm$ 0.0033	Near-frontal; strong source observability
T3	0.1775 $\pm$ 0.0033	5.549 $\pm$ 0.102	0.6796 $\pm$ 0.0062	Lateral temporal; moderate frontal observability
C3	0.1085 $\pm$ 0.0020	3.228 $\pm$ 0.059	0.5779 $\pm$ 0.0084	Central; moderate or low-amplitude observability
Cz	0.0576 $\pm$ 0.0007	1.714 $\pm$ 0.022	0.5088 $\pm$ 0.0144	Central; moderate or low-amplitude observability
C4	0.1119 $\pm$ 0.0012	3.610 $\pm$ 0.040	0.6336 $\pm$ 0.0071	Central; moderate or low-amplitude observability
T4	0.1864 $\pm$ 0.0026	5.830 $\pm$ 0.082	0.6857 $\pm$ 0.0057	Lateral temporal; moderate frontal observability

Channel	nMAE ↓	Raw MAE ( $\mu\text{V}$ )	Pearson $r$ ↑	Observability interpretation
T5	$0.1983 \pm 0.0034$	$6.114 \pm 0.106$	$0.5500 \pm 0.0072$	Posterior/posterior-temporal; weaker phase observability
P3	$0.1493 \pm 0.0033$	$4.470 \pm 0.098$	$0.4574 \pm 0.0066$	Posterior/posterior-temporal; weaker phase observability
Pz	$0.1382 \pm 0.0042$	$4.302 \pm 0.132$	$0.3521 \pm 0.0209$	Posterior/posterior-temporal; weaker phase observability
P4	$0.1734 \pm 0.0035$	$5.191 \pm 0.104$	$0.4399 \pm 0.0079$	Posterior/posterior-temporal; weaker phase observability
T6	$0.2196 \pm 0.0029$	$6.753 \pm 0.089$	$0.5581 \pm 0.0035$	Posterior/posterior-temporal; weaker phase observability

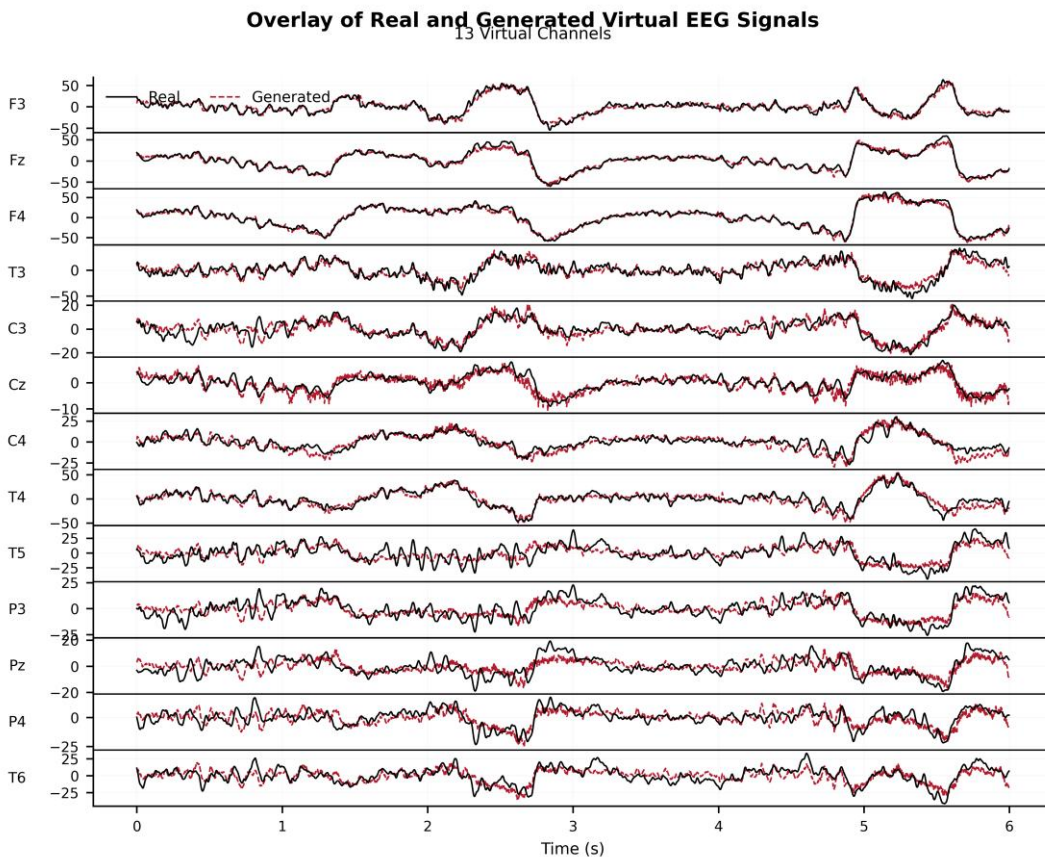


**Fig. 2 Representative overlay of real and generated virtual EEG signals. Generated traces recover broad morphology and local waveform patterns in many targets; posterior targets remain less phase-locked, consistent with weaker frontal observability.**

### 3.3 Spectral organization and ablation evidence

The spectral heatmap comparison in Fig. 3 provides a direct view of the main reconstruction advantage. Real targets contain channel-dependent spectral texture, high-frequency attenuation, and regional differences in energy. FAVC-Net more closely preserved these heterogeneous channel-frequency structures than interpolation baselines and several neural baselines, consistent with the large LSD and KL margins in Table 1.

The spectral comparison is intentionally not reduced to a single averaged number. A low averaged spectral error could still hide channel homogenization or misplaced regional power. By inspecting channel-frequency heatmaps together with LSD and KL, the analysis verifies that the model preserves both the overall spectral envelope and the heterogeneous distribution of energy across virtual

channels. This is important for downstream features such as relative band power, spectral slope, and regional spectral ratios.

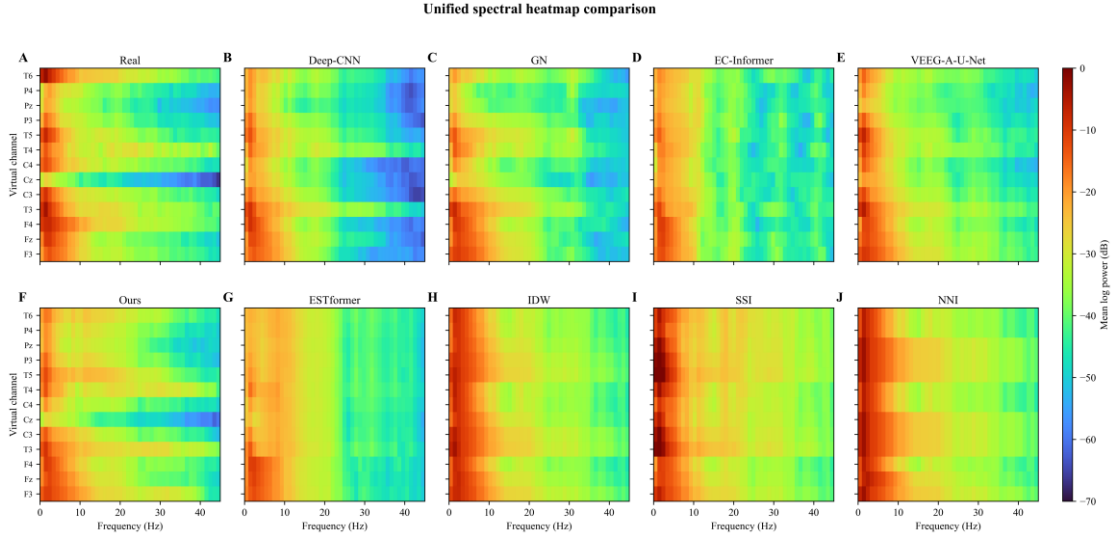


**Fig. 3 Unified spectral heatmap comparison. FAVC-Net preserves global attenuation and channel-dependent spectral texture more closely than interpolation baselines and several neural baselines.**

Ablation results (Table 3 and Fig. 4) identify target-conditioned signed mixing as the dominant mechanism. Removing target-specific attention caused the largest degradation across waveform and spectral metrics, showing that virtual targets require distinct source-response rules. Replacing signed L1 mixing with softmax attention also degraded results, supporting the need for negative and phase-inverted source contributions under common EEG referencing. Removing GATv2 or its spatial prior had smaller but consistent effects, indicating that graph refinement is useful when it regularizes source-block attention rather than directly smoothing output waveforms.

The frequency heatmaps make this point visually: the no-target-specific-attention variant loses much of the structured channel-frequency heterogeneity, whereas the full model better preserves the nonuniform spectral texture of the real targets. The ablations therefore support the architectural rationale rather than only reporting a leaderboard. They show that the main performance gain is produced by target-specific signed source-block mixing, with graph refinement and weak spatial priors acting as stabilizing but not dominant components.

**Table 3 Structural ablation results. Degradation is reported relative to the full FAVC-Net; larger values indicate worse performance after removing the component.**

Ablation setting	MAE degradation (%) $\uparrow$	Pearson r degradation (%) $\downarrow$	LSD degradation (%) $\uparrow$	KL degradation (%) $\uparrow$
No target-specific attention	37.13	46.76	54.25	44.55
Softmax attention	10.07	9.17	3.09	14.11
No GATv2	5.66	5.85	0.79	9.21
GATv2 without spatial prior	4.90	5.29	0.83	5.15
No multi-scale encoder	4.45	5.34	0.83	7.43

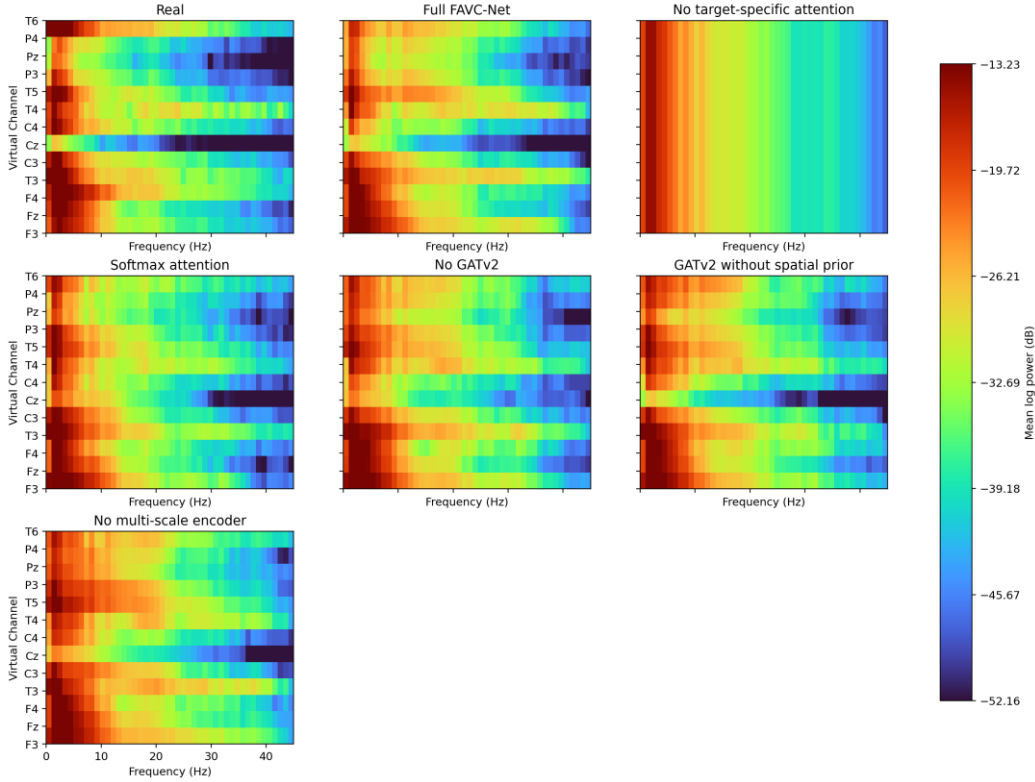


**Fig. 4 Representative frequency heatmaps for real signals and selected ablation groups. The no-target-specific-attention variant shows the strongest loss of channel-frequency organization, supporting target-conditioned source mixing as the central design element.**

### 3.4 Robustness under wearable-like source-channel perturbations

Robustness results strengthen the engineering interpretation of FAVC-Net (Table 4). Across moderate EMG burst, 0.5-s dropout,  $\pm 20\%$  gain mismatch, and moderate mixed stress, FAVC-Net ranked first among all nine methods for LSD, KL, SCI, and CFTC. The largest margins were obtained for spectral fidelity and anti-collapse endpoints. For example, under moderate EMG-like burst contamination, FAVC-Net reduced LSD by 43.6% relative to the best non-FAVC comparator, reduced KL by 46.8%, reduced SCI by 45.9%, and increased CFTC by 4.3%.

The dropout and gain-mismatch conditions test different deployment risks. A 0.5-s dropout approximates transient electrode-contact instability or packet loss, whereas  $\pm 20\%$  gain mismatch approximates impedance, calibration, or device-gain variability. FAVC-Net remained first across all four endpoints in both conditions, indicating that the learned mapping is not merely a fixed-amplitude lookup and does not collapse when one source is briefly unavailable.

The moderate mixed-stress condition is the most deployment-facing test because it combines broadband noise, EMG bursts, short source-channel loss, and gain mismatch. Under this condition, FAVC-Net achieved LSD  $0.874 \pm 0.016$  versus  $1.241 \pm 0.035$  for GN, KL  $0.103 \pm 0.002$  versus  $0.153 \pm 0.007$ , and SCI  $0.026 \pm 0.005$  versus  $0.075 \pm 0.009$ . Subject-level paired Wilcoxon tests showed significantly lower LSD ( $p = 0.00171$ ), KL ( $p = 0.00122$ ), and SCI ( $p = 0.000244$ ) for FAVC-Net, with FAVC-Net better in 92.3%, 84.6%, and 100.0% of subjects, respectively. CFTC was numerically higher (0.920 versus 0.913) but did not reach statistical significance ( $p = 0.216$ ), so it is treated as supporting evidence rather than the main statistical claim.

Table 4. Robustness under wearable-like source-channel perturbations.

Condition	Metric	FAVC rank	FAVC-Net	Best non-FAVC	Improvement
Moderate EMG burst	LSD ↓	#1	0.635 ± 0.010	VEEG-A-U-Net (1.126 ± 0.022)	43.6%
Moderate EMG burst	KL ↓	#1	0.075 ± 0.002	Deep-CNN (0.140 ± 0.007)	46.8%
Moderate EMG burst	SCI ↓	#1	0.034 ± 0.005	GN (0.064 ± 0.009)	45.9%
Moderate EMG burst	CFTC ↑	#1	0.954 ± 0.002	GN (0.915 ± 0.003)	4.3%
0.5-s dropout	LSD ↓	#1	0.578 ± 0.011	VEEG-A-U-Net (0.974 ± 0.014)	40.7%
0.5-s dropout	KL ↓	#1	0.073 ± 0.002	Deep-CNN (0.147 ± 0.008)	50.2%
0.5-s dropout	SCI ↓	#1	0.059 ± 0.007	GN (0.074 ± 0.009)	21.3%
0.5-s dropout	CFTC ↑	#1	0.962 ± 0.002	GN (0.914 ± 0.003)	5.4%
±20% gain mismatch	LSD ↓	#1	0.586 ± 0.011	VEEG-A-U-Net (0.991 ± 0.014)	40.9%
±20% gain mismatch	KL ↓	#1	0.073 ± 0.002	Deep-CNN (0.149 ± 0.008)	51.2%
±20% gain mismatch	SCI ↓	#1	0.058 ± 0.007	GN (0.072 ± 0.009)	19.9%
±20% gain mismatch	CFTC ↑	#1	0.962 ± 0.002	GN (0.913 ± 0.004)	5.4%
Moderate mixed stress	LSD ↓	#1	0.874 ± 0.016	GN (1.241 ± 0.035)	29.6%
Moderate mixed stress	KL ↓	#1	0.103 ± 0.002	GN (0.153 ± 0.007)	33.1%
Moderate mixed stress	SCI ↓	#1	0.026 ± 0.005	GN (0.075 ± 0.009)	65.2%
Moderate mixed stress	CFTC ↑	#1	0.920 ± 0.002	GN (0.913 ± 0.003)	0.8%

SCI, spectral-collapse index; CFTC, channel-frequency texture correlation. Confidence intervals in this table are 95% CIs from subject-level aggregation.

### 3.5 Exploratory external representation transfer

The auxiliary external transfer results are summarized in Table 5. Adding FAVC-generated channels to the real four-channel feature set (D1) improved segment-level AUC over the four-channel baseline (D0) for KNN, Random Forest, and RBF-SVM. D2, which used generated channels only, was also competitive, suggesting that the virtual montage forms a useful transform of the measured frontal signals. Importantly, the negative controls D3 and D4 did not consistently match D1, indicating that the gains are not explained only by adding more columns or by arbitrary pseudo-channel spectra.

The main value of this experiment is not the absolute performance of an external classifier. Rather, it connects reconstruction quality with a realistic engineering use case: a low-channel wearable recording can be transformed into a virtual montage whose spectral-topographic features improve downstream representations under device, montage, sampling-rate, and cohort mismatch. Because the cohort was small and segment-level samples within subject are dependent, these findings are reported as exploratory representation-transfer evidence rather than clinical validation.

**Table 5 Exploratory external representation-transfer check. D0 uses real four-channel features; D1 adds FAVC-generated virtual channels; D2 uses generated channels only; D3 and D4 are dimensionality and pseudo-spectrum controls.**

Classifier	D0 AUC	D1 AUC	D2 AUC	D3 AUC	D4 AUC	D1-D0 AUC	D1 balanced accuracy
KNN	0.6928	0.7528	0.7123	0.7165	0.7209	+0.0600	0.7142
Random Forest	0.6710	0.7369	0.7340	0.6814	0.6770	+0.0659	0.6830
RBF-SVM	0.6472	0.7105	0.6975	0.6697	0.6745	+0.0633	0.6638

Results are segment-level summaries from subject-held-out folds and are reported as exploratory representation-transfer evidence rather than clinical validation.

## 4. Discussion

This study reframes four-frontal virtual EEG channel generation as a dual-domain reconstruction problem. The most important empirical pattern is the separation between modest waveform gains and substantial spectral gains. FAVC-Net does not claim to recover all posterior and parietal phases from four frontal sensors. Instead, it preserves waveform morphology where observable and substantially improves spectral-topographic reliability, which is the form of information most relevant to many wearable EEG features.

The architectural results clarify why the gain occurs. A shared multi-scale encoder extracts compact source representations; source-state embeddings make the source-to-target mapping adaptive to the current window; target-private attention layers give each virtual electrode its own response rule; signed L1 mixing allows negative dependencies; and GATv2 refinement lets neighboring virtual targets exchange information about source-block selection without directly smoothing voltages. The ablation results show that target-specific attention is essential, whereas GATv2 and the spatial prior provide smaller but consistent stabilizing effects. This hierarchy is important because it explains the model as an interpretable sparse-to-dense mapping rather than a large generic neural generator.

The robustness analysis is central to biomedical-engineering relevance. A model trained and tested only under clean public-dataset conditions could be viewed as another offline AI benchmark. Here, perturbations were applied only to the measured source channels, while the target channels remained clean, matching the practical question of whether a wearable system can infer a stable virtual montage from imperfect inputs. The strongest evidence lies in absolute noisy-condition LSD, KL, and SCI. These endpoints show that FAVC-Net is less prone to spectral distortion and channel-frequency collapse under EMG-like bursts, dropout, gain mismatch, and mixed stress.

The channel-wise results define the method's limitations. Frontal targets were highly observable, whereas posterior and parietal targets had weaker phase-sensitive correlation. This should not be hidden because it is a fundamental limitation of sparse sensing. In practice, posterior and parietal virtual channels should be interpreted primarily as frequency-calibrated representations derived from frontal measurements rather than as new independent physiological observations. This observability-aware interpretation reduces the risk of overclaiming and makes the method more suitable for engineering deployment.

The external transfer check is consistent with this interpretation. D1 improvements over D0 suggest that FAVC channels can add useful representation information beyond four frontal features, while negative controls reduce the likelihood that gains arise only from feature-dimensionality expansion. However, the external cohort was small, labels were not used to train the generator, and segment-level samples were subject-dependent. Therefore, the downstream experiment should be read as a bridge between reconstruction and potential application, not as clinical validation.

Several limitations remain. The primary reconstruction experiment used a public task-specific dataset with young adult participants, and broader validation is needed across age ranges, tasks, devices, references, and artifact profiles. The robustness tests were synthetic but wearable-informed; real ambulatory artifact corpora would provide stronger deployment evidence. The method also requires basic quality control of the measured frontal channels and should not be used to infer unobserved physiology when source channels are saturated or missing for long periods. Future work should evaluate uncertainty estimation, online quality gating, prospective wearable recordings, and downstream models trained explicitly to account for virtual-channel reliability.

## 5. Conclusion

FAVC-Net provides a compact frequency-calibrated framework for generating 13 virtual EEG channels from four frontal electrodes. Its main contribution is a robust spectral-topographic reconstruction advantage rather than a claim of perfect waveform recovery. Target-conditioned signed source-block mixing, GATv2 attention refinement, and weak PSD calibration jointly improve spectral

fidelity, reduce spectral-collapse tendency, and preserve useful waveform information. The corrupted-source robustness results further support the method as a practical augmentation module for low-channel wearable EEG systems.

## Declarations

**Funding:** No funding was received for this study.

**Competing interests:** The author declares no competing interests.

**Ethics approval and consent to participate:** The primary reconstruction analysis used the public PRED+CT EEG dataset retrospectively. The exploratory external transfer check used previously collected four-channel EEG recordings from the low-cost wireless EEG measurement system described by Yu and Guo [34]. No new participant recruitment, intervention, or prospective data collection was performed for the present methodological study.

**Data availability:** The primary PRED+CT EEG data used for reconstruction are publicly available through the Patient Repository of EEG Data + Computational Tools (PRED+CT; <https://predict.cs.unm.edu/>), a public EEG repository described at DOI: 10.3389/fninf.2017.00067. The PRED+CT study analyzed here is reported by Cavanagh et al. [4] (DOI: 10.1162/cpsy\_a\_00024). The exploratory external four-channel EEG data are from the low-cost wireless EEG measurement system described by Yu and Guo [34]; access may be provided upon reasonable request to the corresponding author, subject to institutional and ethical restrictions.

**Code availability:** The implementation code, trained checkpoints, and evaluation scripts are available upon request from the corresponding author.

## References

- [1] Bramson B, Meijer S, van Nuland A, Toni I, Roelofs K (2023) Anxious individuals shift emotion control from lateral frontal pole to dorsolateral prefrontal cortex. *Nature Communications* 14:4880
- [2] Brody S, Alon U, Yahav E (2022) How attentive are graph attention networks? In: *International Conference on Learning Representations (ICLR)*
- [3] Buhle JT et al (2014) Cognitive reappraisal of emotion: a meta-analysis of human neuroimaging studies. *Cerebral Cortex* 24:2981-2990
- [4] Cavanagh JF, Bismark AW, Frank MJ, Allen JJB (2019) Multiple dissociations between comorbid depression and anxiety on reward and punishment processing: evidence from computationally informed EEG. *Computational Psychiatry* 3:1-17
- [5] Chen H et al (2024) You Only Acquire Sparse-channel (YOAS): a unified framework for dense-channel EEG generation. *arXiv:2406.15269*
- [6] Cohen MX (2014) *Analyzing Neural Time Series Data: Theory and Practice*. MIT Press, Cambridge
- [7] Corley IA, Huang Y (2018) Deep EEG super-resolution: upsampling EEG spatial resolution with generative adversarial networks. In: *IEEE EMBS International Conference on Biomedical & Health Informatics*, pp 100-103
- [8] Courellis HS, Iversen JR, Poizner H, Cauwenberghs G (2016) EEG channel interpolation using ellipsoid geodesic length. In: *IEEE BioCAS*, pp 540-543
- [9] Delorme A, Makeig S (2004) EEGLAB: an open source toolbox for analysis of single-trial EEG dynamics. *Journal of Neuroscience Methods* 134:9-21
- [10] Donoghue T et al (2020) Parameterizing neural power spectra into periodic and aperiodic components. *Nature Neuroscience* 23:1655-1665
- [11] Ezzi AA, Kamel N, Faye I, Ebenezer EGM (2020) EEG frontal theta-beta ratio and frontal midline theta for the assessment of social anxiety disorder. In: *IEEE ICCSCE*, pp 107-112

- [12] Gramfort A et al (2013) MEG and EEG data analysis with MNE-Python. *Frontiers in Neuroscience* 7:267
- [13] Jasper HH (1958) The ten-twenty electrode system of the International Federation. *Electroencephalography and Clinical Neurophysiology* 10:371-375
- [14] Keil A et al (2014) Committee report: publication guidelines and recommendations for studies using electroencephalography and magnetoencephalography. *Psychophysiology* 51:1-21
- [15] Klimesch W (1999) EEG alpha and theta oscillations reflect cognitive and memory performance: a review and analysis. *Brain Research Reviews* 29:169-195
- [16] Kwon M, Han S, Kim K, Jun SC (2019) Super-resolution for improving EEG spatial resolution using deep convolutional neural network: feasibility study. *Sensors* 19:5317
- [17] Li D, Zeng Z, Wang Z, Yang H (2025) ESTformer: transformer utilising spatiotemporal dependencies for electroencephalogram super-resolution. *Knowledge-Based Systems* 317:113345
- [18] Li LL, Cao GZ, Liang HJ, Chen JC, Zhang YP (2022) EEG generation of virtual channels using an improved Wasserstein generative adversarial networks. In: *Intelligent Robotics and Applications. Lecture Notes in Computer Science*, Springer
- [19] Liu R et al (2023) Assigning channel weights using an attention mechanism: an EEG interpolation algorithm. *Frontiers in Neuroscience* 17:1251677
- [20] Loshchilov I, Hutter F (2019) Decoupled weight decay regularization. In: *International Conference on Learning Representations (ICLR)*
- [21] Nayak S, Tsai AC (2022) Fronto-parietal regions predict transient emotional states in emotion modulated response inhibition via low frequency and beta oscillations. *Symmetry* 14:1244
- [22] Perrin F, Pernier J, Bertrand O, Echallier JF (1989) Spherical splines for scalp potential and current density mapping. *Electroencephalography and Clinical Neurophysiology* 72:184-187
- [23] Pfurtscheller G, Lopes da Silva FH (1999) Event-related EEG/MEG synchronization and desynchronization: basic principles. *Clinical Neurophysiology* 110:1842-1857
- [24] Sanei S, Chambers JA (2007) *EEG Signal Processing*. Wiley, Chichester
- [25] Spielberger CD, Gorsuch RL, Lushene RE, Vagg PR, Jacobs GA (1983) *Manual for the State-Trait Anxiety Inventory*. Consulting Psychologists Press, Palo Alto
- [26] Sun H, Li C, Zhang H (2023) Design of virtual BCI channels based on informer. *Frontiers in Human Neuroscience* 17
- [27] Svantesson M, Olausson H, Eklund A, Thordstein M (2021) Virtual EEG-electrodes: convolutional neural networks as a method for upsampling or restoring channels. *Journal of Neuroscience Methods* 355:109126
- [28] Velickovic P et al (2018) Graph attention networks. In: *International Conference on Learning Representations (ICLR)*
- [29] Welch P (1967) The use of fast Fourier transform for the estimation of power spectra: a method based on time averaging over short, modified periodograms. *IEEE Transactions on Audio and Electroacoustics* 15:70-73
- [30] Yang CK, Guo PC, Zhuang JR (2024) A virtual EEG channels generation method using Attention U-Net. In: *International Conference on System Science and Engineering (ICSSE)*
- [31] Yang CK et al (2026) Attention-enhanced U-Net for sensor-efficient high-density EEG reconstruction in wearable brain monitoring systems. *Journal of Medical Systems*. <https://doi.org/10.1007/s10916-025-02200-4>
- [32] Zhang Y, Yu Y, Li H, Wu A, Zeng L-L, Dewen H (2024) MASER: enhancing EEG spatial resolution with state space modeling. *IEEE Transactions on Neural Systems and Rehabilitation Engineering* 32:3858-3867

[33] Zhou T, Wang S (2025) Generative AI enables EEG super-resolution via spatio-temporal adaptive diffusion learning. *IEEE Transactions on Consumer Electronics* 71:1034-1045

[34] Yu Z, Guo S (2024) A low-cost, wireless, 4-channel EEG measurement system used in virtual reality environments. *HardwareX* 17:e00507. <https://doi.org/10.1016/j.ohx.2024.e00507>